

# Bridging the gap between Monte Carlo simulations and measurements of the LISA Pathfinder test-mass charging for LISA

C. Grimani<sup>1,2</sup>, M. Villani<sup>1,2</sup>, M. Fabi<sup>1,2</sup>, A. Cesarini<sup>2</sup>, and F. Sabbatini<sup>1,2</sup>

<sup>1</sup> DiSpEA, University of Urbino Carlo Bo, Urbino (PU), Italy  
e-mail: catia.grimani@uniurb.it

<sup>2</sup> INFN, Florence, Italy

## ABSTRACT

**Context.** Cubic gold-platinum free-falling test masses (TMs) constitute the mirrors of future LISA and LISA-like interferometers for low-frequency gravitational wave detection in space. High-energy particles of Galactic and solar origin charge the TMs and thus induce spurious electrostatic and magnetic forces that limit the sensitivity of these interferometers. Prelaunch Monte Carlo simulations of the TM charging were carried out for the LISA Pathfinder (LPF) mission, that was planned to test the LISA instrumentation. Measurements and simulations were compared during the mission operations. The measured net TM charging agreed with simulation estimates, while the charging noise was three to four times higher.

**Aims.** We aim to bridge the gap between LPF TM charging noise simulations and observations.

**Methods.** New Monte Carlo simulations of the LPF TM charging due to both Galactic and solar particles were carried out with the FLUKA/LEI toolkit. This allowed propagating low-energy electrons down to a few electronvolt.

**Results.** These improved FLUKA/LEI simulations agree with observations gathered during the mission operations within statistical and Monte Carlo errors. The charging noise induced by Galactic cosmic rays is about one thousand charges per second. This value increases to tens of thousands charges per second during solar energetic particle events. Similar results are expected for the LISA TM charging.

**Key words.** Instrumentation: interferometers – (ISM:) cosmic rays – Sun: particle emission – Elementary particles

## 1. Introduction

The LISA Pathfinder (LPF; Antonucci et al. 2011, 2012; Armano et al. 2016, 2018c) was the European Space Agency demonstrator of the Laser Interferometer Space Antenna (LISA), the first interferometer for gravitational wave detection in space in the frequency range  $2 \times 10^{-5}$ - $10^{-1}$  Hz (Amaro-Seoane et al. 2017). The LPF was launched from the Kourou cosmodrome in French Guyana on December 4, 2015, and reached the Earth-Sun system Lagrange point L1 at the end of January 2016. The mission ended on July 18, 2017. The LPF spacecraft (S/C) consisted of one S/C carrying two cubic gold-platinum test masses (TMs) of approximately 2 kg mass, playing the role of mirrors of the interferometer. The aim of the LPF mission was to study the sources of noise that are expected to limit the sensitivity of LISA. The most relevant sources of noise (Castelli 2020) are: a) a frequency-independent Brownian noise due to the residual gas pressure in the region close to the TMs; b) an actuation noise, associated with the TMs that are kept at the center of an electrode housing by actuation electrodes. This noise is dominant below 1 mHz and is proportional to  $f^{-1}$ , where  $f$  represents the frequency here and below; c) an interferometer sensing noise relevant above 10 mHz and proportional to  $f^2$ ; d) a low-frequency fluctuation of the average stray electrostatic fields below 1 mHz, proportional to  $f^{-1}$ ; e) laser radiation pressure that is mainly relevant below 1 mHz and f) Poissonian noise associated with the TM charging. This noise appears dominant below 1 mHz and is proportional to  $f^{-1}$ . Finally, to these sources of noise, the noise due to the expected stochastic background of Galactic white

dwarf binaries must be added. This is relevant around 1 mHz (confusion noise, Ruiter et al. 2010).

Spurious Coulomb and magnetic forces between the TMs and surrounding electrodes were predicted to originate from the charging process of the TMs due to Galactic and solar particles with energies higher than 100 MeV/n. A detailed study of the noise associated with TM net and effective charging was carried out before the LPF launch for both LPF and LISA (Shaul et al. 2005). The measurement of the charging noise carried out with LPF appears in Figure 3.11 of Castelli (2020). Estimates and measurements appear to vary as a function of frequency and range between  $2 \times 10^{-16}$  and  $2 \times 10^{-15}$   $\text{m s}^{-2} \text{Hz}^{-0.5}$  between  $10^{-5}$  Hz and  $10^{-4}$  Hz. In order to limit the intensity of the forces that increase with the charge deposited on the TMs, a periodic discharging with ultraviolet light beams illuminating the electrode housing was carried out on board the LPF S/C (Armano et al. 2018b). An analogous discharging process will be considered for LISA (Inchauspé et al. 2020).

Prelaunch Monte Carlo simulations carried out to estimate the net and effective charging (charging noise) of the LPF TMs during the mission operations (Grimani et al. 2004; Vocca et al. 2004; Grimani et al. 2005; Vocca et al. 2005; Araújo et al. 2005; Wass et al. 2005; Grimani et al. 2015) were carried out with the FLUKA (Battistoni et al. 2014; Böhlen et al. 2014) and Geant4 (Agostinelli et al. 2003; Allison et al. 2006, 2016) toolkits by considering the same satellite geometry. These two sets of simulations agreed excellently when the same input particle fluxes were considered. It is worthwhile to recall that the net charging is given by the algebraic sum of the charges deposited on the TMs, while positively and negatively charged particles contribute to

the effective charging. Measurements of the TM charging carried out with LPF in April 2016 (Armano et al. 2017) showed that the net charging agreed with the simulations, while the effective charging appeared higher by a factor of 3 to 4. Several possibilities were explored to determine the origin of this mismatch. It was evaluated that any cause associated with the satellite geometry and incident particle fluxes would have generated a disagreement between observations and simulations common to the net and effective charging. Conversely, the experimental evidence suggested that a large number of particles with the same charge were entering and escaping the TMs and thus contributed to the charging noise without significantly increasing the net charging. This scenario is consistent with a large number of very low-energy electrons that are produced by primary and secondary particles escaping the surface of the TMs and surrounding electrodes. In the FLUKA and Geant4 versions available before the LPF mission launch, the propagation of electrons was limited to 1 keV and 250 eV, respectively. In the majority of applications, this low-energy limit in the electron propagation does not affect the results of the simulations because the paths of these particles in dense material such as gold are very limited, they are on the order of microns at most. However, in the case of future space interferometers where the potential difference between electrodes and TMs is approximately one volt, the role of very low-energy electrons cannot be neglected. In this paper we report the results of recent improved simulations. A new Monte Carlo code was written in order to include the propagation of very low-energy electrons escaping the electrodes and the TMs. This dedicated Fortran 90 Monte Carlo tool called Low Energy Ionization (LEI, Villani et al. 2020; Grimani et al. 2021b; Villani et al. 2021) was used in combination with FLUKA. Ionization energy losses, kinetic emission, and quantum backscattering are considered in LEI. The net and effective charging for LPF in 2016 are re-estimated here. On the basis of lessons learned with the LPF, reasonable expectations for the TM charging induced by Galactic cosmic rays (GCRs) and solar particles for LISA TMs are also presented. In Sections 2 and 3, the Galactic and solar particle environment for LPF and LISA are discussed. In Section 4, the net and effective TM charging simulations and measurements are presented. In Section 5, the FLUKA/LEI Monte Carlo tools are described. In Section 6, the Monte Carlo program uncertainties are discussed. Finally, in Section 7, the new simulation results are compared to LPF observations.

## 2. Galactic and solar particle fluxes

An average of  $13.8 \text{ g cm}^{-2}$  of S/C and instrument material surrounded the LPF TMs. A similar amount of material is expected to be found on board the LISA TMs. This average material thickness sets the minimum energy of hadrons and electrons that contribute to the TM charging to 100 MeV/n and 20 MeV, respectively. The GCRs and solar energetic particles (SEPs) associated with gradual events (Reames 2022) typically lie in this energy range. Both cosmic rays and SEPs consist approximately of 90% protons, 8% helium nuclei, 1% heavy nuclei, and 1% electrons, where the percentages are meant in particle numbers to the total number. The overall GCR flux was observed to vary by a factor of 4 in the inner heliosphere during the last three solar cycles (Grimani et al. 2021a). The cosmic-ray intensity presents quasi 11-year and quasi 22-year periodicities that are associated with the solar activity and the global solar magnetic field (GSMF) polarity change. The LPF satellite was sent into orbit during the declining phase of solar cycle 24, which was characterized by a positive polarity period of the GSMF. The same is expected for

LISA, which is scheduled to be launched in 2035 near the maximum of solar cycle 26 (Singh & Bhargawa 2019). Grimani et al. (2008) showed that during positive polarity periods, the energy spectra,  $J(r, E, t)$ , of cosmic rays at a distance  $r$  from the Sun at a time  $t$  are well represented by the symmetric model in the force field approximation by Gleeson & Axford (G&A; 1968). By assuming time-independent interstellar cosmic-ray intensities  $J(\infty, E + \Phi)$  and an energy loss parameter  $\Phi$ , it is found that

$$\frac{J(r, E, t)}{E^2 - E_0^2} = \frac{J(\infty, E + \Phi)}{(E + \Phi)^2 - E_0^2}, \quad (1)$$

where  $E$  and  $E_0$  represent the particle total energy and rest mass, respectively. For  $Z=1$  particles with a rigidity (particle momentum per unit charge) higher than 100 MV, the effect of the solar activity is completely defined by the solar modulation parameter  $\phi$ , which at these energies is equal to  $\Phi$  (Grimani et al. 2009, and references therein). The proton and helium interstellar spectra adopted in this work are reported in Burger et al. (2000) and Shikaze et al. (2006), respectively. The solar modulation parameter, estimated on the basis of the Burger et al. (2000) proton interstellar spectrum, was reconstructed from ground-based cosmic-ray data.<sup>1</sup> Unfortunately, no helium energy spectrum at the interstellar medium is reported in Burger et al. (2000).

The particle spectra obtained with the G&A model were parameterized according to the following equation:

$$F(E) = \frac{A}{(E + b)^\alpha} E^\beta \text{ Particles (m}^2 \text{ sr s GeV n}^{-1}\text{)}^{-1}, \quad (2)$$

where the parameter  $b$  allows us to modulate the spectra at low energies, and the parameters  $\alpha$  and  $\beta$  set the trend at high energies. Finally,  $A$  is the normalization constant. The agreement of equation 2 with the G&A model was discussed in Armano et al. (2018a) and references therein.

Before the LPF launch, predictions of proton and helium fluxes were carried out for the first part of the mission operations on the basis of the expected minimum and maximum solar activity for the period corresponding to a solar modulation parameter ranging between 350 MV/c and 800 MV/c (details are reported in Grimani et al. 2015). This estimate was carried out on the basis of observations gathered in the past during similar solar modulation conditions. In Table 1 we report the parameters  $A$ ,  $b$ ,  $\alpha$  and  $\beta$  that appear in equation 2 for the LPF prelaunch predictions. The energy spectra are shown in Figure 1. In the same table and figure, we also report the parameters and the particle spectra estimated for Bartels rotation (BR) 2492 between March 31, 2016, and April 26, 2016, when the TM charging measurements were carried out in space. We recall that the BR number corresponds to the number of 27-day rotations of the Sun since February 8, 1832.

The proton and helium fluxes estimated with the G&A model for BR 2492 when the solar modulation parameter  $\phi^2$  was 468 MV/c were compared with the AMS-02 experiment data gathered on the Space Station above 450 MeV/n and published in 2018 (Aguilar et al. 2018) after the LPF mission was accomplished. The model-predicted proton flux appears to agree well with the data, while the helium flux is about 25% higher. As a result, in Table 1, Figure 1, and in the simulations, we adopted the helium flux normalized on the AMS-02 data. The different

<sup>1</sup> [http://cosmicrays.oulu.fi/phi/Phi\\_mon.txt](http://cosmicrays.oulu.fi/phi/Phi_mon.txt)

<sup>2</sup> [http://cosmicrays.oulu.fi/phi/Phi\\_mon.txt](http://cosmicrays.oulu.fi/phi/Phi_mon.txt)

results of the model obtained for proton and helium energy spectra are ascribed to the helium flux at the interstellar medium reported in (Shikaze et al. 2006), which would require solar modulation parameters higher than those considered above.

In Tables 2 and 3 and Figures 2-4, our predictions for proton, nucleus, and electron energy spectra for LISA are presented. The LISA mission is supposed to be sent to space in 2035 at the maximum of solar cycle 26, for which the actual solar activity is unknown at present. As a result, we considered a solar modulation parameter of  $\phi=200$  MV/c at solar minimum and  $\phi=1200$  MV/c at solar maximum as extreme cases.

In order to disentangle the contribution of  $^3\text{He}$  and  $^4\text{He}$  isotopes from the overall He flux to the TM charging, in Figure 3 we show the  $^3\text{He}/^4\text{He}$  ratio measured by the IMAX (Labrador et al. 2003), SMILI (Beatty et al. 1993), PAMELA (Adriani et al. 2016), and AMS-02 (Aguilar et al. 2019) experiments. These observations were gathered at minimum and maximum solar modulation conditions and different GSMF polarity. On the basis of the  $^3\text{He}/^4\text{He}$  data and models discussed in Reimer et al. (1998); Ngobeni et al. (2022), we considered the parameterizations reported in Tables 4 and 5 and in Figure 3. Unfortunately, for the  $^3\text{He}/^4\text{He}$  ratio and the flux of nuclei with atomic number ( $Z$ )  $>2$ , no model can be considered reliable enough to estimate the particle energy spectra during intermediate solar modulation periods due to the limited amount of data gathered in space. In particular, model predictions introduce uncertainties larger than the contribution of these particles to the TM charging. As a result, for the simulations carried out for the BR 2492, we considered the overall helium flux as consisting of  $^4\text{He}$  only, and the contribution of nuclei with  $Z>2$  was estimated from solar minimum and maximum conditions (Papini et al. 1996). These considerations do not apply to electrons that have been measured by different experiments over several dozen years down to tens of MeV (see for instance Grimani 2004, 2007; Adriani et al. 2011; Weng et al. 2016).

The Galactic and interplanetary electron contribution to the LPF TM charging was discussed in detail in Grimani et al. (2009). The overall electron flux includes one Galactic component above approximately 100 MeV, one solar component below a few MeV associated with both impulsive and gradual solar events, and one Jovian component mainly below 20 MeV. Because particles below 20 MeV are not energetic enough to reach and charge the TMs, we considered only Galactic electrons. After proper modulation at 1 AU, the electron energy spectrum at the interstellar medium by Moskalenko & Strong (1998, shown with the dotted line in Figure 4,) was found to nicely represent observations gathered near Earth for different conditions of solar modulation and during different epochs of the GSMF (Grimani 2004, 2007). As a result, the electron spectra at 1 AU at solar minimum ( $\phi=200$  MV/c; dashed line in Figure 4), at solar maximum ( $\phi=1200$  MV/c; continuous line in Figure 4), and during BR 2492 ( $\phi=468$  MV/c; dot-dashed line in Figure 4) were estimated for LISA and LPF with the G&A model and the interstellar spectrum by Moskalenko & Strong (1998). For the comparison of the simulated and measured LPF TM charging during BR 2492, we have considered the proton, helium, and electron energy spectra reported in Tables 1 and 6. The preliminary minimum and maximum estimates of the LISA TM net and effective charging were estimated by considering the LPF satellite geometry and solar minimum and maximum conditions for cosmic-ray protons, helium, carbon, nitrogen, oxygen, iron nuclei (Papini et al. 1996), and electrons (Grimani et al. 2009).

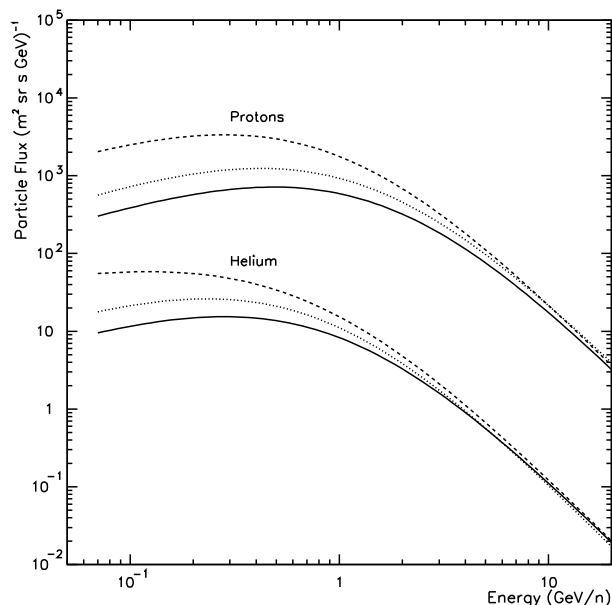


**Fig. 1.** Minimum (continuous lines) and maximum (dashed lines) proton and helium cosmic-ray energy spectra estimated for LPF before the mission launch (December 2015). The dotted lines indicate the cosmic-ray proton and helium energy spectra for BR 2492, a few months after launch. The helium energy spectra have been scaled down by a factor of ten to avoid superposed lines.

### 3. Solar energetic particle events during LISA

Solar particle fluxes evolve in space, energy, and time during the events. The parameterization of the solar particle energy spectra during different events was discussed, for instance, in Grimani et al. (2013). In the majority of cases, the SEP energy spectra, at the onset of the events, show a power-law trend with an exponential cutoff, while at the peak, they appear compatible with a power-law function. Moreover, at the onset of SEP events, electrons are observed first due to particle velocity dispersion, and the particle spatial distribution is characterized by small pitch angles with respect to the interplanetary magnetic field lines for magnetically well-connected events. Conversely, during the declining phase of the events, the spatial particle distribution becomes isotropic. Impulsive SEP events are associated with proton acceleration below 50 MeV (Reames 2021) and play no role in the TM charging. Unfortunately, during the LPF operations, no gradual SEP events were observed above the GCR background. We have considered here the LPF TM charging at the onset and at the peak of gradual SEP events of different intensities observed on February 23, 1956 (Vashenyuk et al. 2007), December 13, 2006, and December 14, 2006 (Adriani et al. 2011), in order to obtain reasonable TM charging estimates for LISA. The proton fluxes observed during the evolution of these events are shown in Figure 5. The 2006 events were observed in space by the PAMELA experiment, and the proton differential fluxes of the February 23, 1956, event were inferred from neutron monitor data. The probability of intense events such as the one on February 23, 1956, characterized by a proton fluence of  $10^9$  protons  $\text{cm}^{-2}$  above 30 MeV, is one event every 60 years (Miroshnichenko & Nymmik 2014). This event is considered here as a worst case for LISA. The fluence of most of the gradual SEP events ranges between  $10^6$  and  $10^7$  protons  $\text{cm}^{-2}$

**Table 1.** LPF prelaunch minimum (top panel) and maximum (middle panel) cosmic-ray energy spectrum predictions. The parameterizations were carried out according to the function  $F(E)=A(E+b)^{-\alpha}E^\beta$  particles ( $\text{m}^2 \text{sr s GeV n}^{-1}$ )<sup>-1</sup>. Estimates of the cosmic-ray energy spectra in April 2016, when the TM charging measurements were carried out with LPF, are reported in the bottom panel.

Minimum cosmic-ray flux predictions for LPF ( $\phi=800$ MV/c)				
Particle	A	b	$\alpha$	$\beta$
p	18000	1.54	3.67	0.88
He	850	0.91	3.60	0.85
Maximum cosmic-ray flux predictions for LPF ( $\phi=350$ MV/c)				
Particle	A	b	$\alpha$	$\beta$
p	18000	0.88	3.68	0.89
He	850	0.7	3.23	0.48
Cosmic-ray flux during the LPF mission operations in April 2016 ( $\phi=468$ MV/c)				
Particle	A	b	$\alpha$	$\beta$
p	18000	1.25	3.66	0.92
He	850	0.74	3.68	0.85

**Table 2.** Parameterizations of proton and nucleus energy spectra at 1 AU at solar minimum ( $\phi=200$  MV/c) and maximum ( $\phi=1200$  MV/c).

Particle	Solar minimum				Solar maximum			
	A	b	$\alpha$	$\beta$	A	b	$\alpha$	$\beta$
Protons	18000	0.65	3.66	0.87	18000	2.17	3.66	0.87
Helium	850	0.99	3.10	0.35	850	2.17	3.10	0.35
Carbon	28	1.05	3.25	0.50	28	1.15	3.75	1.00
Nitrogen	7.3	1.05	3.25	0.50	7.3	1.15	3.75	1.00
Oxygen	25.2	1.05	3.25	0.50	25.2	1.15	3.75	1.00
Iron	2.3	1.05	3.25	0.50	2.3	1.15	3.75	1.00

**Table 3.** Parameterization of electron energy spectra at solar minimum and solar maximum.

Solar minimum	
Energy range	Parameterization
> 20 MeV	$400(E + 0.82)^{-3.66}E^{0.5}$
Solar maximum	
Energy range	Parameterization
50 MeV - 1 GeV	$4.5(E - 0.04)^{0.84}$
> 1 GeV	$400(E + 2.5)^{-3.66}E^{0.5}$

**Table 4.**  $^3\text{He}/^4\text{He}$  ratio parameterization at solar minimum.

Energy range (GeV/n)	$^3\text{He}/^4\text{He}$
0.07-0.197	$0.44219 E^{-0.94664}$
0.197-0.415	$0.23439 E^{0.5559}$
0.415-1.778	$0.1859 E^{0.29248}$
1.778-2.67	0.22
2.67-7	$0.277756 E^{-0.2374}$
7-13.40	$0.277756 E^{-0.2374}$
> 13.40	0.15

above 30 MeV. The SEP events with fluences of  $10^5$ - $10^6$  protons  $\text{cm}^{-2}$  are not observed at solar minimum above the background of GCRs above 70 MeV. On the basis of observations gathered during previous solar cycles<sup>3</sup> and predictions for the next two cycles (Singh & Bhargawa 2019), the expected number of SEP events during the LISA operations will range between 10 and 20 per year at most during the first part of the mission because the LISA launch is scheduled at the maximum of solar cycle 26.

**Table 5.**  $^3\text{He}/^4\text{He}$  ratio parameterization at solar maximum.

Energy range (GeV/n)	$^3\text{He}/^4\text{He}$
0.07-0.197	$0.195943 E^{0.49625}$
0.197-1.	$0.14375 E^{0.3056}$
1.-2.254	$0.14375 E^{0.102597}$
2.254-7.	$0.16089 E^{-0.036}$
> 7	0.15

<sup>3</sup> <https://wwwbis.sidc.be/silso/datafiles>

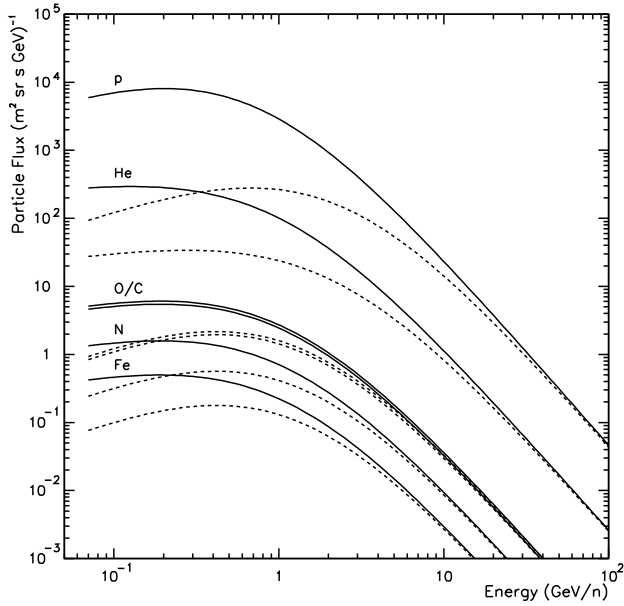


**Fig. 2.** Cosmic-ray energy spectra at solar minimum ( $\phi = 200$  MV/c; continuous lines) and solar maximum ( $\phi = 1200$  MV/c; dashed lines). From top to bottom are reported the energy spectra of protons (p), helium (He), carbon (C), oxygen (O), nitrogen (N), and iron (Fe) nuclei.

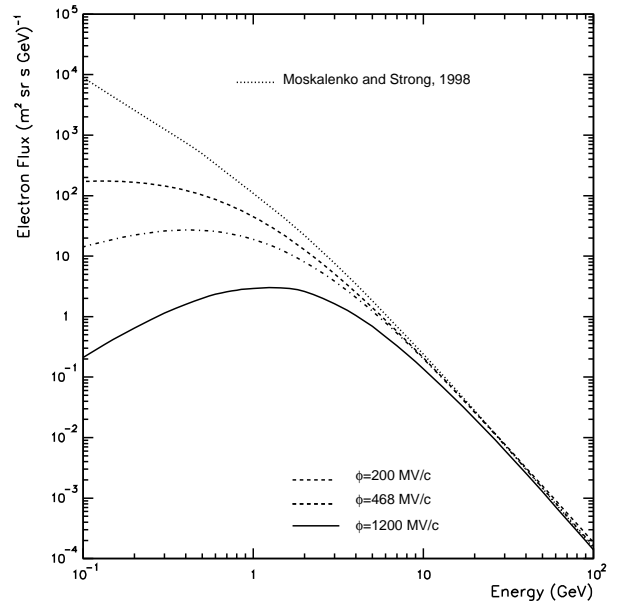


**Fig. 4.** Galactic electron energy spectra at solar minimum (dashed line), solar maximum (continuous line) and during the BR 2492 (dot-dashed curve). The interstellar spectrum is represented by the top dotted line (Grimani 2004, 2007, and references therein).

**Table 6.** Same as Table 3 for Galactic electrons during BR 2492.

$A$	$b$	$\alpha$	$\beta$
670	1.25	4.4	1.1

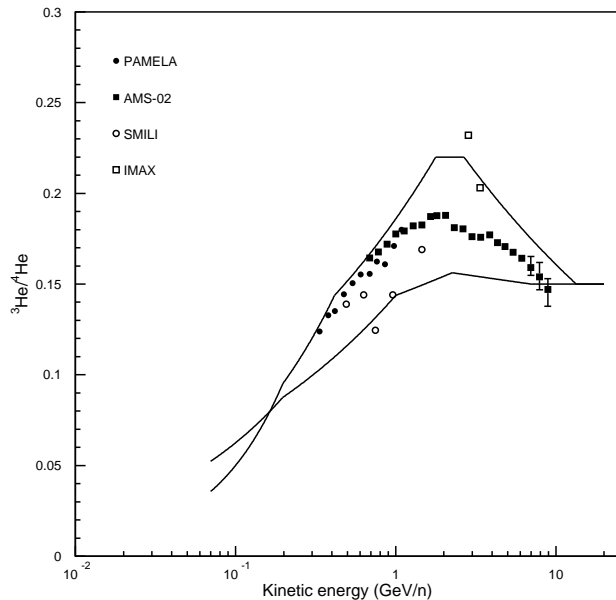


**Fig. 3.**  ${}^3\text{He}^4\text{He}$  parameterization at solar minimum (top curve) and maximum (bottom curve). Data were gathered by the IMAX (Labrador et al. 2003), SMILI (Beatty et al. 1993), PAMELA (Adriani et al. 2016), and AMS-02 (Aguilar et al. 2019) experiments.

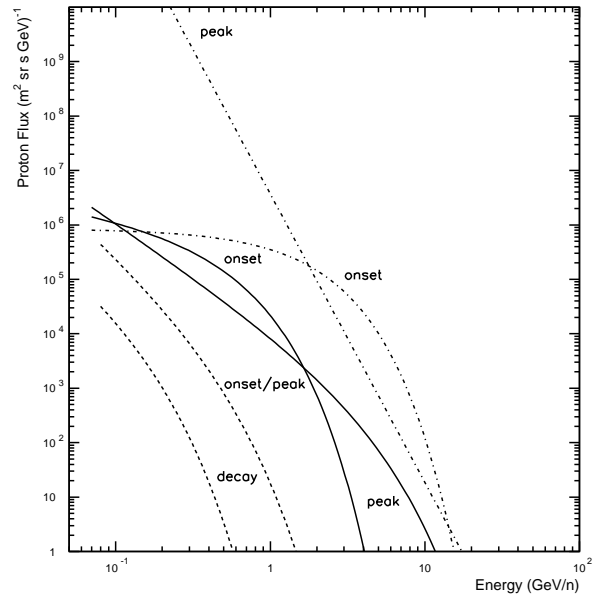


**Fig. 5.** Solar energetic proton fluxes observed during the evolution of the gradual events dated February 23, 1956 (dot-dashed line), December 13, 2006 (continuous line), and December 14, 2006 (dashed line). The onset, peak, and decay phases of each event are indicated.

#### 4. LISA Pathfinder net and effective TM charging

The net ( $\lambda_{net}$ ) and effective ( $\lambda_{eff}$ ) charging rates of the LPF TMs are defined below. They are

$$\lambda_{net} = \sum_{j=-\infty}^{+\infty} j\lambda_j \text{ s}^{-1} \quad (3)$$

$$\lambda_{eff} = \sum_{j=-\infty}^{+\infty} j^2 \lambda_j \text{ s}^{-1}, \quad (4)$$

where  $j$  represents the net number of positive and negative charges deposited by single events, and  $\lambda_j$  is the rate of occurrence of these events. As we pointed out above, positive and negative charges cancel out in the net charging computation, while both positive and negative net deposited charges contribute to the effective charging. The spectral density of the charging shot noise ( $S$ ) is expressed in terms of effective charging rate,

$$S = \sqrt{2e^2 \lambda_{eff}} \text{ e s}^{-1} \text{ Hz}^{-0.5}, \quad (5)$$

where  $e$  is the elementary charge.

#### 4.1. Lisa Pathfinder prelaunch TM charging Monte Carlo simulations

Monte Carlo simulations of the LPF TM charging were formerly carried out with Geant4 and FLUKA for different conditions of solar modulation several years before the mission launch (Grimani et al. 2004; Vocca et al. 2004; Grimani et al. 2005; Vocca et al. 2005; Araújo et al. 2005; Wass et al. 2005). New Monte Carlo simulations based on FLUKA were performed in 2015 just before mission launch by considering as input cosmic-ray fluxes the fluxes that were estimated on the basis of the expected minimum and maximum solar activity at the end of 2015 and beginning of 2016 presented in Section 2 (Grimani et al. 2015). The TM charging obtained with these input fluxes appears in Table 7. FLUKA and Geant4 simulations returned very similar results at solar minimum, as discussed in detail in Grimani et al. (2015), even though the energy limit for particle propagation in the two simulation codes was different and limited for electrons, positrons, and photons to 1 keV in FLUKA and to 250 eV in Geant4. This evidence was ascribed to the average ionization potential in gold of 790 eV (Villani et al. 2020), to which the secondary electron production and propagation was limited de facto in Geant4.

#### 4.2. LISA Pathfinder TM charging during mission operations

The TM net and effective charging were measured on board the LPF satellite on April 20-23, 2016. The results are reported in Table 8 (Armano et al. 2017).

Comparison of Tables 7 and 8 show that the measured net charging is in the middle of the prediction range, while the effective charging appears three to four times higher than expected. Any possible cause for the mismatch had to be plausibly associated with particles with the same charge sign entering and escaping the TMs, thus contributing to the noise without contributing to the net charging. Electrons and positrons, as the lowest-mass charged particles, propagate at keV energies over typical path-lengths of tens of microns in solid materials. When the propagation of these particles is considered below 1 keV, ionization energy losses, multiple scattering, and quantum backscattering must be considered properly. As a result, the computation time strongly increases, and consequently, it is in general neglected. In the majority of applications, the limited propagation lengths of these particles at low energies do not impact the results. Unfortunately, this is not the case of the LPF and LISA missions because the potential difference between the TMs and surrounding electrodes is about one volt and low-energy electrons strongly

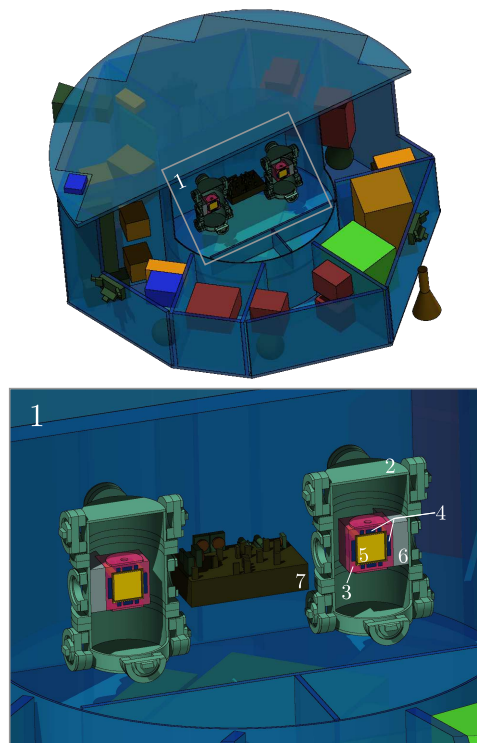


**Fig. 6.** LPF combinatorial geometry model built with Flair for FLUKA: 1 LISA technology package, 2 vacuum enclosure, 3 electrode housing, 4 electrodes, 5 test mass, 6 gravitational compensation mass, and 7 optical bench. Items 2 to 7 are found around both TMs.

affect the TM charging process. The low-energy electron propagation in the Geant4 toolkit currently depends on the libraries adopted in the simulations. In particular, the electron production and propagation is limited to 100 eV (Ivanchenko et al. 2017) in Geant4/opt 4.

## 5. FLUKA/LEI tool

The LPF geometry has been built in FLUKA with the Flair interface (Vlachoudis 2009, see Fig. 6). The electron and positron production and propagation from keV energies down to the limit of their quantum wave-like behavior has been taken into account in a new Monte Carlo program written in Fortran 90, LEI, in order to include the effects of very low-energy electromagnetic processes in the LPF TM charging simulations. The LEI Monte Carlo has been activated in the outer 150 nm of the gold-plated layers of the TMs and electrodes. The thickness of these layers was chosen as a compromise between increasing computing time and the aim to include all the electrons and positrons contributing to the TM net and effective charging in the simulations. In our simulation architecture, incoming primary and secondary particles are propagated with FLUKA down to the 150 nm gold layers. All charged particles incident on the gold layers constitute the input data for the Monte Carlo LEI, which allows us to simulate electron and positron low-energy electromagnetic processes down to 12 eV when the diffraction is also activated (see Villani et al. 2020; Grimani et al. 2021b; Villani et al. 2021, for details). The low-energy electromagnetic processes included in the LEI Monte Carlo are discussed below.

Particles incident on the electrode and TM gold-plated layers are propagated by considering one nanometer step, while the electrons produced within the slab are propagated at one angstrom step. The program code is available upon request.

**Table 7.** LPF prelaunch minimum (left) and maximum (right) TM charging predictions for the first part of the mission (Grimani et al. 2015).

Particle	Net charging	Effective charging rate	Net charging	Effective charging rate
	(e <sup>+</sup> s <sup>-1</sup> )	(s <sup>-1</sup> )	(e <sup>+</sup> s <sup>-1</sup> )	(s <sup>-1</sup> )
Protons	14.1	168.9	32.5	295.5
<sup>3</sup> He	0.22	0.92	1.9	5.6
<sup>4</sup> He	0.81	1.9	3.8	10.7

**Table 8.** Net and effective TM charging measured with LPF on April 20-23, 2016 (Armano et al. 2017).

	Test mass 1	Test mass 2
Net charging (e <sup>+</sup> s <sup>-1</sup> )	+22.9 ± 1.7	+24.5 ± 2.1
Effective charging rate (s <sup>-1</sup> )	1060 ± 90	1360 ± 130

When the FLUKA/LEI simulations are complete, all charged particles deposited into the TMs by each incident particle are counted and the net and effective charging are estimated.

### 5.1. Low-energy particle ionization in LEI

When charged particles propagate through matter, the target material atoms are ionized. Low-energy ionization in the range 12-1000 eV was implemented in LEI. For all particles different from electrons (ions, pions, muons, etc.), we adopted the formula by Cucinotta et al. (1996) to calculate the number of electrons produced per kinetic energy interval,

$$\frac{dn}{dK} = \frac{2\pi N e^4 Z_s^2}{mc^2 \beta^2 K^2} \left[ 1 - \frac{\beta^2 K}{E_m} + \frac{\pi \beta Z_s^2}{137} \sqrt{\frac{K}{E_m}} \left( 1 - \frac{K}{E_m} \right) \right] dx, \quad (6)$$

where  $N$  is the material electron density,  $\beta$  is the incoming particle velocity,  $e$ ,  $m$ , and  $K$  are the emitted electron charge, mass, and kinetic energy, and  $dx$  is the material thickness traversed by the incident particle. The maximum energy that can be transferred to an emitted electron is

$$E_m = \frac{2mc^2 \beta^2}{1 - \beta^2}, \quad (7)$$

while the effective charge of the particle inside the material is given by

$$Z_s = Z \left[ 1 - \exp\left(-\frac{125\beta}{Z^{2/3}}\right) \right], \quad (8)$$

where  $Z$  is the charge of the incident particle. The ionized electron direction emission is finally estimated as follows:

$$\cos \theta = \sqrt{\frac{K}{E_m}}, \quad (9)$$

where  $\theta$  is the angle between the direction of the ionizing particle and that of the emitted electron.

For electron-induced ionization, we adopted the cross section reported below (Sakata et al. 2016),

$$\sigma = \frac{4\pi a_0^2 \alpha^4 N_s}{(\beta_i^2 + (\beta_u^2 + \beta_b^2)/v) 2b'} \left[ \frac{1}{2} \left( \ln\left(\frac{\beta_i^2}{1 - \beta_i^2}\right) - \beta_i^2 - \ln(2b') \right) \left( 1 - \frac{1}{t'} \right) + 1 - \frac{1}{t} - \frac{\ln(t)}{t+1} \frac{1+2t'}{(1+t'/2)^2} + \frac{b'^2}{(1+t'/2)^2} \frac{t-1}{2} \right]. \quad (10)$$

In the above formula,

$$\beta_t^2 = 1 - \frac{1}{(1+t')^2} \quad t' = \frac{K}{mc^2}, \quad (11)$$

$$\beta_u^2 = 1 - \frac{1}{(1+u')^2} \quad u' = \frac{U}{mc^2}, \quad (12)$$

$$\beta_b^2 = 1 - \frac{1}{(1+b')^2} \quad b' = \frac{B}{mc^2}, \quad (13)$$

$$t = \frac{K}{B}, \quad (14)$$

where  $K$  is the incident electron kinetic energy,  $U$  is the bound kinetic energy of the electron inside the atom,  $B$  is the bound electron binding energy,  $N_s$  is the occupation number of the shell to be ionized, and  $\alpha$  is the fine structure constant. Finally,  $v$  is an empirical parameter set equal to the principal quantum number of the atomic shell to be ionized.

Ionization contributes most to the low-energy electron production (Villani et al. 2020). Kinetic emission and quantum backscattering balance out the effect of ionization, leading to a positive net charge of the TMs while increasing the effective charging.

### 5.2. Kinetic emission

Electron emission may follow when a particle below keV energies crosses a material slab. If the incoming particle is an ion, this process is called ion-induced electron emission (IIEE), while if it is an electron it is called electron-induced electron emission (EIEE): we refer to both processes as kinetic emission.

Kinetic emission is the macroscopic effect of many microscopic processes such as plasmon production and decay and both elastic and inelastic scattering (Grimani et al. 2021b). The overall electron production is represented by the yield, that is, by the number of electrons emitted per incoming particle. In Grimani et al. (2021b), we calculated the expected electron yield for IIEE and EIEE from gold by using the Schou approach (Schou 1980). We found that for EIEE, the peak of electron emission is at about 100 eV, while for IIEE, the maximum emission occurs at higher energies for an increasing atomic mass number  $A$  of the incident ion, and also that this maximum increases with the ion charge  $Z$ .

The kinetic emission process has been implemented in LEI using the yield: Whenever an electron hits the surface of the TM, a number of electrons corresponding to the yield for that energy is emitted from the surface according to Grimani et al. (2021b). The role of electrons that elastically backscattered before reaching the TMs above 1 keV was also taken into account in FLUKA Kim et al. (2015).

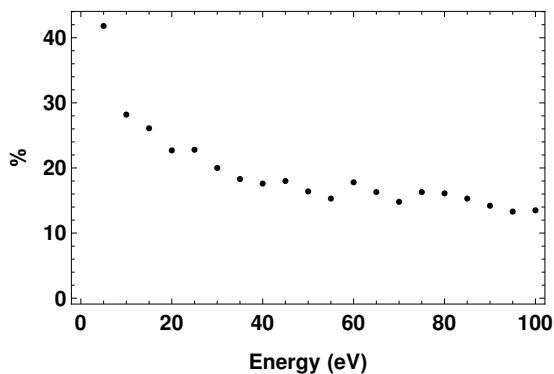


**Fig. 7.** Quantum backscattering probability for electrons and positrons incident on a gold slab as a function of the energy.

### 5.3. Electron and positron quantum backscattering

The electron and positron quantum particle-wave duality cannot be neglected below 12 eV. As a result, quantomechanical effects such as quantum backscattering and diffraction are included in the simulation.

The probability of backscattering is calculated by estimating the scattering amplitude. This calculation for gold was carried out in [Grimani et al. \(2021b\)](#) by solving the Schrödinger equation for  $e^-$  and  $e^+$  propagating inside the lattice of a gold crystal. We found that the probability of these particles being backscattered strongly depends on their energy and decreases from about 42% at 5 eV to about 13% at 100 eV, as shown in Figure 7.

## 6. FLUKA and LEI Monte Carlo simulation uncertainties

The Monte Carlo simulation results are affected by statistical and systematic uncertainties associated with the number of simulated events and the parameterizations of the physical processes. For each run, about two million events were simulated. The statistical errors were kept below 10% and 5% on the net and effective TM charging, respectively. Further improving of these statistical uncertainties would have been meaningless because of the Monte Carlo intrinsic uncertainties. The comparison of the FLUKA Monte Carlo outcomes and beam experiment data discussed in [Lechner et al. \(2019\)](#) has shown that the Monte Carlo outcomes are consistent with observations within 10%. The LEI uncertainties are discussed below for each process.

### 6.1. Ionization

In Figures 8 and 9, our parameterization of the number of secondary electrons produced by ionizing 2 MeV and 1 GeV protons propagating through a gold slab of 150 nm thickness is compared to [Tanabashi et al. \(2018\)](#). The two parameterizations agree well: only a small deviation is observed above 100 keV for 1 GeV incident protons.

The parameterization for electron production by ionization reported in [Cucinotta et al. \(1996\)](#) was previously adopted by [Kobetich & Katz \(1968\)](#), who compared the model to experimental data in lead and gold. They reported good agreement.

The validation of the cross section adopted in LEI for electron energy losses through ionization is discussed in [Sakata et al. \(2016\)](#). They found that the uncertainty on the ionization cross section above 1 keV, where both ionization and bremsstrahlung dominate, appears to be a few percent because data and model

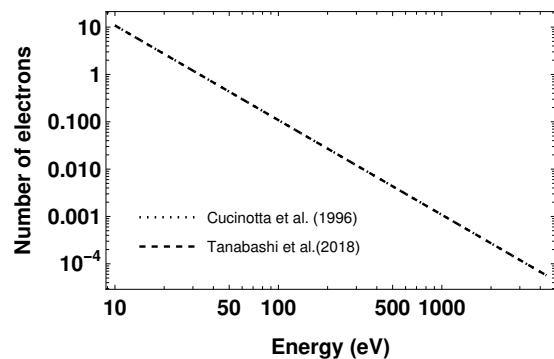


**Fig. 8.** Comparison of the number of electrons produced by 2 MeV protons incident on a 150 nm gold slab according to [Cucinotta et al. \(1996\)](#) and [Tanabashi et al. \(2018\)](#). The two models overlap perfectly.

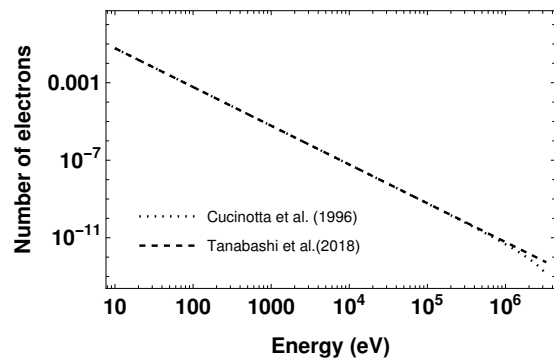


**Fig. 9.** Same as Figure 8 for 1 GeV protons.

overlap within the data errors. No experimental data are available below 1 keV for comparison in [Sakata et al. \(2016\)](#).

### 6.2. Kinetic emission

The electron yield for carbon, nitrogen, and oxygen nuclei incident on a gold slab inferred from [Eder et al. \(1999\)](#) was compared with our calculations reported in [Grimani et al. \(2021b\)](#) and implemented in LEI. We point out that [Eder et al. \(1999\)](#) did not use fully ionized incoming atoms, retaining one electron, while in our calculations, the atoms were considered fully ionized. The overall difference of the yield was of 15% for IIEE. Conversely, the electron yield associated with EIEE estimated according to [Schou \(1980\)](#) exceeds the recent experimental work by [Azzolini et al. \(2019\)](#) by 30%.

### 6.3. Quantum backscattering

In [Grimani et al. \(2021b\)](#) we calculated the probability of quantum backscattering from a slab of gold for incident electrons with energies lower than 100 eV. Experimental electron backscattering data below 100 eV are reported in [Jablonski et al. \(1993\)](#), who calculated the backscattering probability also for several elements, including gold. The probability of backscattering in gold appears to increase at low energies as in our calculations; in particular, based on their results, we estimated a backscattering probability of about 26% at 50 eV. In fair agreement, we have found 20% at 50 eV. An overall 10% uncertainty on quantum backscattering yield was set as a result. Because low-energy electrons escape the gold-plated layers from electrodes toward the TMs and vice versa, these uncertainties con-



stitute upper limits to those that actually affect the calculations of the net and effective charging.

## 7. Lisa Pathfinder in-orbit test-mass charging and FLUKA/LEI simulations

The final geometry and material distribution of LISA S/C is not yet available. However, based on the preliminary design, it is plausible to assume that the material grammage of the LISA and LPF S/C will be similar. In order to set a range of reasonable values of the expected TM charging for LISA, we carried out new simulations with the FLUKA/LEI toolkit of the LPF TM charging at solar minimum, maximum, and during BR 2492 in order to compare these new simulation outcomes with the measurements carried out with LPF in April 2016. The cosmic-ray input fluxes are reported in Figures 1-4. The results of the simulations appear in Tables 9-11. Table 9 shows that at solar minimum and maximum, the main contribution to the TM net and effective charging is given by protons. Helium and heavy nuclei increase the net charging by a few percent and the effective charging at solar minimum and maximum by about 50%, even though they constitute just about 10% of the cosmic-ray sample. This result arises because the large production of electrons by ionization increases with the square of the nucleus charge. On the other hand, we confirmed that a large number of low-energy secondary electrons that escape TMs and electrodes contribute only little to the net TM charging. The GCR electrons, representing only 1% of the cosmic-ray sample, lower the net charging by about 15% and increase the effective charging by approximately 10%.

In the simulations for BR 2492, during the declining phase of solar cycle 24, the contribution of nuclei with  $Z > 2$  to the net and effective charge is estimated from Table 9 as an average between solar minimum and maximum conditions. As we recalled above, nucleus flux models at intermediate solar modulation conditions would introduce uncertainties larger than the contribution of each of these nuclei to the net TM charging. We estimate that nuclei account for net and effective charging of 2-4% and 10-20% of the total, respectively. The slightly negative charging associated with heavy nuclei is due to statistical fluctuations in the low-energy electron production.

The simulation results reported in Tables 10 and 11 for the two TMs can be compared with the TM net and effective charging measurements carried out with LPF in April 2016. They are listed in Table 8. Our simulations agree excellently with observations when the heavy nuclei contribution is taken into account and within the measurements and Monte Carlo uncertainties discussed in the previous sections. Moreover, the contribution of the low-energy electromagnetic physics is highly important to estimate the LPF TM effective charging. Our work allows us to bridge the gap between Monte Carlo simulations and observations for LISA.

During the LPF mission, no SEP events were observed. In order to estimate the possible effects on LISA, the charging of the LPF TMs was calculated for the three SEP events of different intensities dated February 23, 1956, December 13, 2006, and December 14, 2006, as reported in Section 3. The TM charging at the onset and peak of each event is reported in Table 12. The charging of the TMs during the evolution of these SEP events increases by several orders of magnitude with respect to that induced by GCRs. These estimates will be useful to optimize the TM discharging process during the LISA operations.

## 8. Conclusions

High-energy particles of solar and Galactic origin will charge the TMs of the future interferometers for gravitational wave detection in space. Monte Carlo simulations carried out with Geant4 and FLUKA toolkits before the LPF launch allowed us to estimate the net and effective charging for the first part of the mission (end of 2015 to the beginning of 2016) on the basis of the expected solar activity. Measurements carried out with LPF in April 2016 were compared to simulations. The observed net charging of about 23-25 positive charges per second agreed with expectations, while the estimated charging noise was three to four times lower than in-orbit observations. This mismatch probably arises because low-energy electromagnetic processes below 1 keV are missing in FLUKA.

The results of new LPF TM charging simulations are reported in this work. A dedicated Monte Carlo (LEI) was written to include low-energy electron propagation and quantum backscattering down to a few electronvolt. These new simulations appear to agree with the observations within the errors of the Monte Carlo simulation and measurements. We also considered solar minimum and solar maximum conditions and SEP events for LPF as reasonable predictions for the TM charging of LISA. The details of the LISA S/C geometry are not yet available, even though the amount of material surrounding the TMs is expected to be similar to that of LPF. The net (effective) charging will probably vary between a few (hundreds) and about 50 (thousand) charges per second due to GCRs. The charging is estimated to increase by several orders of magnitude during SEP events. The evolution of three SEP events with a fluence ranging between  $10^6$  and  $10^9$  protons  $\text{cm}^{-2}$  was considered. The net and effective charging induced by cosmic rays differ by a few orders of magnitude, while during SEP events, the net and effective charging are similar because the SEP energy spectra present higher spectral indices above hundreds of MeV with respect to GCRs. As a result, the majority of particles stop in the material surrounding the TMs or in the TMs with a minor secondary particle production due to cascading, which increases the effective charging more than the net charging. The LISA TM charging estimates will allow us to control the TM charging process, to optimize the discharging during the mission operations, and to evaluate the role of the charging noise with respect to the total mission noise budget.

*Acknowledgements.* Part of this work was funded under the European Space Agency project AO-1-10081 - TEST MASS CHARGING TOOLKIT AND LPF LESSONS LEARNED.

## References

- Adriani, O., Barbarino, G. C., Bazilevskaia, G. A., et al. 2011, *ApJ*, 742, 102
- Adriani, O., Barbarino, G. C., Bazilevskaia, G. A., et al. 2011, *Phys. Rev. Lett.*, 106, 201101
- Adriani, O., Barbarino, G. C., Bazilevskaia, G. A., et al. 2016, *ApJ*, 818, 100
- Agostinelli, S., Allison, J., Amako, K., et al. 2003, *Nuclear Instruments and Methods in Physics Research Section A: Accelerators, Spectrometers, Detectors and Associated Equipment*, 506, 250
- Aguilar, M., Ali Cavasonza, L., Alpat, B., et al. 2018, *Phys. Rev. Lett.*, 121, 051101
- Aguilar, M., Ali Cavasonza, L., Ambrosi, G., et al. 2019, *Phys. Rev. Lett.*, 123, 181102
- Allison, J., Amako, K., Apostolakis, J., et al. 2006, *IEEE Transactions on Nuclear Science*, 53, 270
- Allison, J., Amako, K., Apostolakis, J., et al. 2016, *Nuclear Instruments and Methods in Physics Research Section A: Accelerators, Spectrometers, Detectors and Associated Equipment*, 835, 186
- Amaro-Seoane, P., Audley, H., Babak, S., et al. 2017, arXiv e-prints, arXiv:1702.00786

**Table 9.** Average FLUKA/LEI LPF TM charging at solar minimum and solar maximum for LISA.

Primary particle	Solar Minimum		Solar Maximum	
	Net charging ( $e^+ s^{-1}$ )	Effective charging rate ( $s^{-1}$ )	Net charging ( $e^+ s^{-1}$ )	Effective charging rate ( $s^{-1}$ )
Protons	50.4	937.9	5.30	316.6
$^4\text{He}$	5.8	182.5	0.28	108.9
$^3\text{He}$	2.9	90.5	0.07	54.0
Nitrogen	-0.1	11.3	0.02	6.4
Carbon	0.4	31.9	0.08	19.6
Oxygen	0.5	80.6	0.13	34.0
Iron	0.1	27.5	-0.04	26.5
Electrons	-7.8	167.8	-1.2	53.6
Total	52.2	1530.0	4.64	619.6

**Table 10.** FLUKA/LEI LPF first TM charging during the BR 2492.

Primary particle	Net charging ( $e^+ s^{-1}$ )	Effective charging rate ( $s^{-1}$ )
Protons	21.35	611.8
Helium	3.9	201.2
Electrons	-4.1	75.5
Total	21.15	888.5

**Table 11.** Same as Table 10 for the second LPF TM.

Primary particle	Net charging ( $e^+ s^{-1}$ )	Effective charging rate ( $s^{-1}$ )
Protons	20.5	673.6
Helium	5.8	161.9
Electrons	-4.3	98.0
Total	22.0	933.5

**Table 12.** Average FLUKA/LEI LPF TM charging during the evolution of SEP events.

02/23/1956		
	Net charging ( $e^+ s^{-1}$ )	Effective charging rate ( $s^{-1}$ )
Onset	8870	73730
Peak	$1.3 \times 10^8$	$1.3 \times 10^8$
12/13/2006		
	Net charging ( $e^+ s^{-1}$ )	Effective charging rate ( $s^{-1}$ )
Onset	2425	5695
Peak	1123	2360
12/14/2006		
	Net charging ( $e^+ s^{-1}$ )	Effective charging rate ( $s^{-1}$ )
Peak	88.7	141.3
Decay	3.3	4.9

- Antonucci, F., Armano, M., Audley, H., et al. 2011, CQG, 28, 094001  
Antonucci, F., Armano, M., Audley, H., et al. 2012, CQG, 29, 124014  
Araújo, H. M. et al. 2005, Astr. Phys., 22, 451  
Armano, M., Audley, H., Auger, G., et al. 2016, Phys. Rev. Lett., 116, 231101  
Armano, M., Audley, H., Auger, G., et al. 2017, Phys. Rev. Lett., 118, 171101  
Armano, M., Audley, H., Baird, J., et al. 2018a, ApJ, 854, 113  
Armano, M., Audley, H., Baird, J., et al. 2018b, Phys. Rev. D, 98, 062001  
Armano, M., Audley, H., Baird, J., et al. 2018c, Physical Review Letters, 120, 061101  
Azzolini, M., Angelucci, M., Cimino, R., et al. 2019, Journal of Physics Condensed Matter, 31, 055901  
Battistoni, G., Boehlen, T., Cerutti, F., et al. 2014, in Joint International Conference on Supercomputing in Nuclear Applications + Monte Carlo, 06005  
Beatty, J. J., Ficenec, D. J., Tobias, S., et al. 1993, ApJ, 413, 268  
Böhlen, T. T., Cerutti, F., Chin, M. P. W., et al. 2014, Nuclear Data Sheets, 120, 211  
Burger, R. A., Potgieter, M. S., & Heber, B. 2000, Journal of Geophysical Research: Space Physics, 105, 27447  
Castelli, E. 2020, PhD thesis, University of Trento, [10.15168/11572\_254388]  
Cucinotta, F. A., Katz, R., Wilson, J. W., & Dubey, R. R. 1996, in American Institute of Physics Conference Series, Vol. 362, Two-center effects in ion-atom Collisions: A Symposium in honor of M. Eugene Rudd, 245–265  
Eder, H., Aumayr, F., & Winter, H. 1999, Nuclear Instruments and Methods in Physics Research B, 154, 185  
Gleeson, L. J. & Axford, W. I. 1968, ApJ, 154, 1011  
Grimani, C. 2004, A&A, 418, 649  
Grimani, C. 2007, A&A, 474, 339  
Grimani, C., Andretta, V., Chioetto, P., et al. 2021a, A&A, 656, A15  
Grimani, C., Cesarini, A., Fabi, M., & Villani, M. 2021b, CQG, 38, 045013  
Grimani, C., Fabi, M., Finetti, N., Laurenza, M., & Storini, M. 2013, in Journal of Physics Conference Series, Vol. 409, Journal of Physics Conference Series, 012159  
Grimani, C., Fabi, M., Finetti, N., & Tombolato, D. 2008, International Cosmic Ray Conference, 1, 485  
Grimani, C., Fabi, M., Finetti, N., & Tombolato, D. 2009, CQG, 26, 215004  
Grimani, C., Fabi, M., Lobo, A., Mateos, I., & Telloni, D. 2015, CQG, 32, 035001  
Grimani, C., Vocca, H., Bagni, G., et al. 2005, CQG, 22, S327  
Grimani, C., Vocca, H., Barone, M., et al. 2004, CQG, 21, S629  
Inchauspé, H., Olatunde, T., Apple, S., et al. 2020, Phys. Rev. D, 102, 042002  
Ivanchenko, V., Dondero, P., Fioretti, V., et al. 2017, Experimental Astronomy, 44, 437  
Jablonski, A., Jansson, C., & Tougaard, S. 1993, Phys. Rev. B, 47, 7420  
Kim, S. H., Pia, M. G., Basaglia, T., et al. 2015, IEEE Transactions on Nuclear Science, 62, 451  
Kobetich, E. J. & Katz, R. 1968, Physical Review, 170, 391  
Labrador, A. W., Yanasak, N. E., Binns, W. R., et al. 2003, in International Cosmic Ray Conference, Vol. 4, International Cosmic Ray Conference, 1773  
Lechner, A., Auchmann, B., Baer, T., et al. 2019, Phys. Rev. Accel. Beams, 22, 071003  
Miroshnichenko, L. I. & Nymmik, R. A. 2014, Radiation Measurements, 61, 6  
Moskalenko, I. V. & Strong, A. W. 1998, Ap. J., 493, 694  
Ngobeni, M. D., Ngobeni, D., Potgieter, M., et al. 2022, in 37th International Cosmic Ray Conference. 12-23 July 2021. Berlin, 1338  
Papini, P., Grimani, C., & Stephens, S. 1996, Nuovo Cim., C19, 367

- Reames, D. V. 2021, Solar Energetic Particles. A Modern Primer on Understanding Sources, Acceleration and Propagation, Vol. 978
- Reames, D. V. 2022, arXiv e-prints, arXiv:2203.15886
- Reimer, O., Menn, W., Hof, M., et al. 1998, ApJ, 496, 490
- Ruiter, A. J., Belczynski, K., Benacquista, M., Larson, S. L., & Williams, G. 2010, ApJ, 717, 1006
- Sakata, D., Incerti, S., Bordage, M. C., et al. 2016, Journal of Applied Physics, 120, 244901
- Schou, J. 1980, Phys. Rev. B, 22, 2141
- Shaul, D. N. A., Araújo, H. M., Rochester, G. K., Sumner, T. J., & Wass, P. J. 2005, Classical and Quantum Gravity, 22, S297
- Shikaze, Y. et al. 2006, astro-ph/0611388 [astro-ph/0611388]
- Singh, A. K. & Bhargawa, A. 2019, Ap&SS, 364, 12
- Tanabashi, M., Hagiwara, K., Hikasa, K., et al. 2018, Phys. Rev. D, 98, 030001
- Vashenyuk, E. V., Balabin, Y. V., Gvozdevsky, B. B., & Miroshnichenko, L. I. 2007, Bulletin of the Russian Academy of Sciences, Physics, 71, 933
- Villani, M., Benella, S., Fabi, M., & Grimani, C. 2020, Applied Surface Science, 512, 145734
- Villani, M., Cesarini, A., Fabi, M., & Grimani, C. 2021, CQG, 38, 145005
- Vlachoudis, V. 2009, in International Conference on Mathematics, Computational Methods & Reactor Physics (M&C 2009), Saratoga Springs, New York, 790–800
- Vocca, H., Grimani, C., Amico, P., et al. 2004, CQG, 21, S665
- Vocca, H., Grimani, C., Amico, P., et al. 2005, CQG, 22, S319
- Wass, P. J., Araújo, H. M., Shaul, D. N. A., & Sumner, T. J. 2005, CQG, 22, S311
- Weng, Z. L., Vagelli, V., & AMS Collaboration. 2016, Nuclear and Particle Physics Proceedings, 273-275, 466